Compact Multi-Band Filter/Diplexer LNAs Using Split-Type Multi-Resonant Stages

Steven Matthew Cheng, *Graduate Student Member, IEEE*, and Dimitra Psychogiou, *Senior Member, IEEE*

***Abstract*— paper reports on the design and practical development of RF co-designed low-noise amplifiers (LNAs) with multi-band RF filter and diplexer capabilities. Split-type multi-resonant stages are used as complex-terminated matching networks to functionalize new classes of multi-band filtering LNAs (MBF-LNAs) and multi-band diplexer LNAs (MBD-LNAs). In this manner, the need for conventional matching networks or additional RF filtering is eliminated in the RF front-end, thus reducing its size. Miniaturization is further enhanced using split-type multi-resonant stages that are smaller than conventional transversal resonator arrays or filter-banks of in-line coupled resonators. The MBF-LNA and the MBD-LNA concepts are validated in S-band through the realization of two dual-band MBF-LNAs (MBF-LNA I and MBF-LNA II) and a quad-band MBD-LNA. Specifically, the MBF-LNA I exhibited a low noise figure (NF) of 0.65/0.9 dB and a gain of 19.1/16.5 dB for its passbands centered at 2.5/3.29 GHz. The MBFLNA II exhibited significantly higher isolation between the two passbands of 79.5 dB while having a NF of 1/1.5 dB and gain of 18.3/15.9 dB at 2.57/3.26 GHz. The MBD-LNA demonstrated two dual-band output channels with Channel 1 having a NF of 0.92/0.93 dB and gain of 17.2/15.2 dB at 2.38/3.29 GHz and Channel 2 having a NF of 0.82/1.02 dB and gain of 16.8/14.2 dB at 2.82/3.8 GHz.**

***Index Terms*— Bandpass filter, co-design, diplexer, filter amplifier, low noise amplifier, multi-band.**

I. Introduction

FUTURE 5G+/6G wireless communication systems will need to provide connectivity to an ultra-high number of applications, users and data rates. However, this is very challenging due to the scarceness of spectrum at the FR1 band (0.41-7.125 GHz) and the lack of RF transceivers able to support multiple bands or weak RF signals in the presence of strong interferers that desensitize the RF receiver [1], [2], [3], [4], [5]. As such, recent research efforts are focusing on the realization of multi-band (MB) RF components such as filters [6], [7], [8], [9], [10], [11], power dividers [12], phase shifters [13] and low noise amplifiers (LNAs) [14], [15], [16], [17], [18], [19], [20], [21], [22], [23], [24], [25], [26], [27], [28], [29], [30], [31], [32], [33], [34], [35], [36] with filters and LNAs being the most popular ones due to being the very first components in the receiver chain; thus, the most crucial for the signal to noise ratio (SNR).

Multi-band LNAs (MB-LNAs) can be realized in many different ways: i) using reconfigurable circuitry [15], [16], [17], [18], [19], [20], [21] or ii) by acquiring a very wide part of the spectrum [22], [23], [24], [25], [26], or iii) utilizing concurrent multi-band networks [27], [28], [29], [30], [31], [32], [33], [34], [35], [36]. In terms of reconfigurable circuitry approaches, a cascode LNA configuration operating within five sub-bands of the 1.8-5.0 GHz spectrum is demonstrated in [15] having a noise figure (NF) below 0.7 dB. However, band reconfigurability is not incorporated within the circuitry leading to manual replacement of the matching networks (MNs). The MB-LNAs in [16], [17], and [18] used switchable input and output MNs and the switchless LNA approach in [20] is reconfigured by only changing the biasing of the transistor. Specifically, [16] implemented separate MNs and transistors at the input for each band while the output is implemented with a switched capacitor-based resonator. This facilitated reconfigurable operation of 24 GHz, 28 GHz, and 39 GHz with a high average NF of 5.1 dB. To minimize the NF, the switch at the input is replaced with a dual-band input matching network (IMN) as in [17] and [18]. However, due to the use of switches at the output matching network (OMN), inherent losses and increased footprint were observed. Switch losses can be removed using the switchless approach in [20] wherein a coupled-line diplexer is used to split the low frequency and high frequency bands along two transistor paths achieving an average NF of 4.35 dB at 39 GHz and 48 GHz. However, additional transistors are added entailing higher power consumption and circuit size. Moreover, all these approaches aren't truly MB but rather reconfigurable-band due to only being able to acquire one band at a time.

Wideband LNAs able to cover a wide range of bands have also been discussed. Notable demonstrations include the use of multi-resonant IMNs [25] or a combination of a dual-resonant IMN and a transformer-based OMN in [26]. The concept in [25] was able to achieve an average NF of 3.75 dB from 16.5 GHz to 44.5 GHz while an average NF of 3.3 dB was obtained between 27 GHz and 46 GHz in [26]. Although these approaches are able to achieve low NF across a wide range of frequencies, potential interferers within unused bands of the wideband spectrum aren't filtered and are prone to desensitize the RF receiver. Thus, additional single- or multi-band RF filters need to be added before or after these LNAs.

Manuscript received 29 April 2024; revised 9 July 2024; accepted 15 July 2024. This work was supported by the Science Foundation Ireland (SFI) under Grant 20/RP/8334 and Grant 13/RC/2077. This article was recommended by Associate Editor R. Garg. *(Corresponding author: Steven Matthew Cheng.)*

The authors are with the School of Engineering, University College Cork, Cork, T12 K8AF Ireland, and also with the Advanced RF Technology Group, Tyndall National Institute, Cork, T12 R5CP Ireland (e-mail: steven.cheng@tyndall.ie; Dpsychogiou@ucc.ie).

Color versions of one or more figures in this article are available at https://doi.org/10.1109/TCSI.2024.3430376.

Digital Object Identifier 10.1109/TCSI.2024.3430376

Concurrent multi-band LNAs have also been reported [27], [28], [29], [30], [31], [32], [33], [34], [35], [36]. Specifically, in dual-band LNA realizations, dual-band IMNs and OMNs are employed using series and parallel resonances [27], [28], [29], [30], [31]. This approach has been demonstrated using a lumped-element PCB integration approach in [30] operating at 1.1 GHz and 2.4 GHz and using a GaAs implementation [31] with two operational ranges centered at 26 GHz and 48 GHz. However, these dual-band LNAs exhibited low selectivity and poor filtering characteristics. To improve filtering selectivity, alternative dual-band LNA concepts were discussed in [33] and [34]. In [33], a double shunt stub IMN and a dual-band step impedance resonator together with an additional MN at the output of the transistor were used. In this manner, a dual-band LNA having an average NF of 3.4 dB at 2.4 GHz and 5.7 GHz was demonstrated. However, the input return loss of the device was below 5 dB resulting in poor matching and inefficient power transfer from source to load. In yet another approach, a step impedance low-pass filter was used at the OMN of the transistor suppressing the high frequency spurs [34] and showing an average NF of 0.9 dB for 2.45 GHz and 5.25 GHz. However, each of the passbands exhibited variable gain characteristics. With regards to the realization of higher number of bands, a tri-band load comprising a wide-band load and two notch filters was utilized at the transistor's output together with a wideband IMN [35]. It demonstrated three bands centered at 13.5 GHz, 24 GHz, and 35 GHz with an average NF of 3.45 dB; however, it had poor filtering selectivity. In [36], a quad-band LNA was realized using a dual-band IMN and two notch filters. However, it exhibited poor selectivity, and it wasn't validated experimentally.

To address the challenges of selectivity or concurrent operation in multiple bands, RF co-designed filter-amplifiers using complex-matched filtering MNs are increasingly explored to facilitate RF filtering while eliminating the need for IMNs/OMNs [37], [38], [39], [40]. A substrate integrated waveguide (SIW) BPF co-designed with LNA functionality wherein filter MNs are used at the output [38], input [39] or both input and output [40] has been demonstrated at X band. However, these implementations result in large overall circuit size due to being based on waveguide integration technologies. A microstrip-based BPF MN was demonstrated in [41], where mixed coupling was exploited to improve the filter's selectivity through the introduction of transmission zeros (TZs). Although this technique reduced the overall size of the BPF-LNA and resulted in a low NF of 2.26 dB, this approach can't be easily scaled for the realization of multi-band transfer functions.

Considering the lack of MB-LNAs with highly-selective filtering capabilities, this manuscript presents for the first time a method to realize compact MBF-LNAs and MBD-LNAs with pre-described filtering selectivity that is easily scalable to high order transfer functions (TFs) and multiple bands. The proposed concept shown in Fig. 1 (a) uses as a basis split-type complex-matched multi-resonant filtering networks that are directly attached to the input and/or output of low-noise transistor. Furthermore, the manuscript demonstrates how the split-type multi-resonant concept illustrated in Fig. 1 (b) can be exploited for the realization of multi-band diplexer LNA

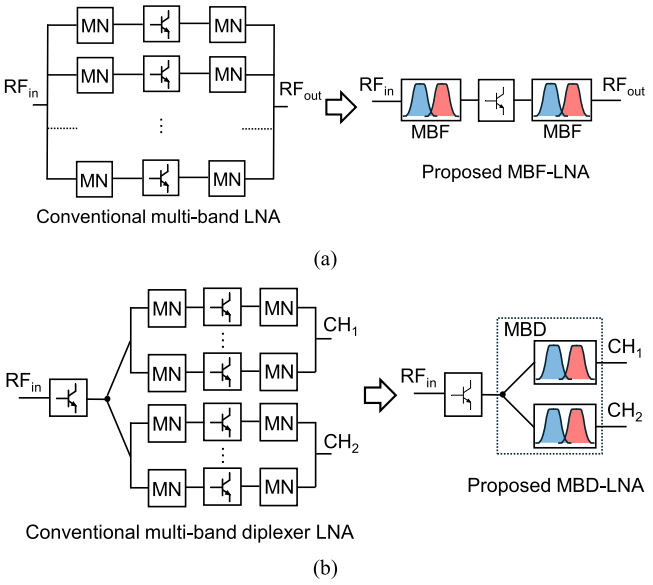

Fig. 1. Conceptual block diagram of the proposed multi-band filter LNA (MBF-LNA) and multi-band diplexer LNA (MBD-LNA) concepts. (a) Conventional and proposed MBF-LNA using complex-terminated split–type multi-resonant matching networks that are directly attached to a low noise transistor. (b) Conventional and proposed MBD-LNA using complex-terminated split-type multi-resonant diplexer matching networks that are directly attached to a low noise transistor.

(MBD-LNA) that are presented in this work for the first time. The outline of this paper is as follows. Section II discusses the operating principles of the split-type complex-matched filtering concept. The design methodology for the MBF-LNA and MBD-LNA are discussed in Section III. The practical validation of the concept is presented in Section IV. Finally, the relevant contributions of this work are presented in Section V.

II. Split-Type Filter Matching Network

The coupling routing diagram (CRD) of the split-type MN is presented in Fig. 2(a). It is shaped by N in-series cascaded M-band multi-resonant split-type stages. Each stage comprises M resonators that exhibit a TF shaped by M poles and M-1 TZs. Thus, the entire multi-stage split-type multi-band filter matching network (MBF-MN) can facilitate M N-pole passbands that are separated with $N\cdot(M\text{-}1)$ TZs [42]. Overall, the split-type configuration can be understood as a filtering MN that creates a wide passband—created by the in-line resonators (grey circles) that is divided up in multiple bands through TZs that are generated by the in-parallel resonators (black circles).

To determine the pole and TZ locations, the $n+2$ coupling matrix of the filter is first derived using the coupling matrix synthesis in [43], [44], [45], [46], and [47] and they are then specified from the S-parameters after being calculated using (1)-(4).

$$S_{21} = -2j\,[A]^{-1}_{n+2,1} \tag{1}$$

$$S_{11} = 1 + 2j\,[A]^{-1}_{1,1} \tag{2}$$

$$Z_{in} = \frac{1 - S_{11}}{1 + S_{11}} \tag{3}$$

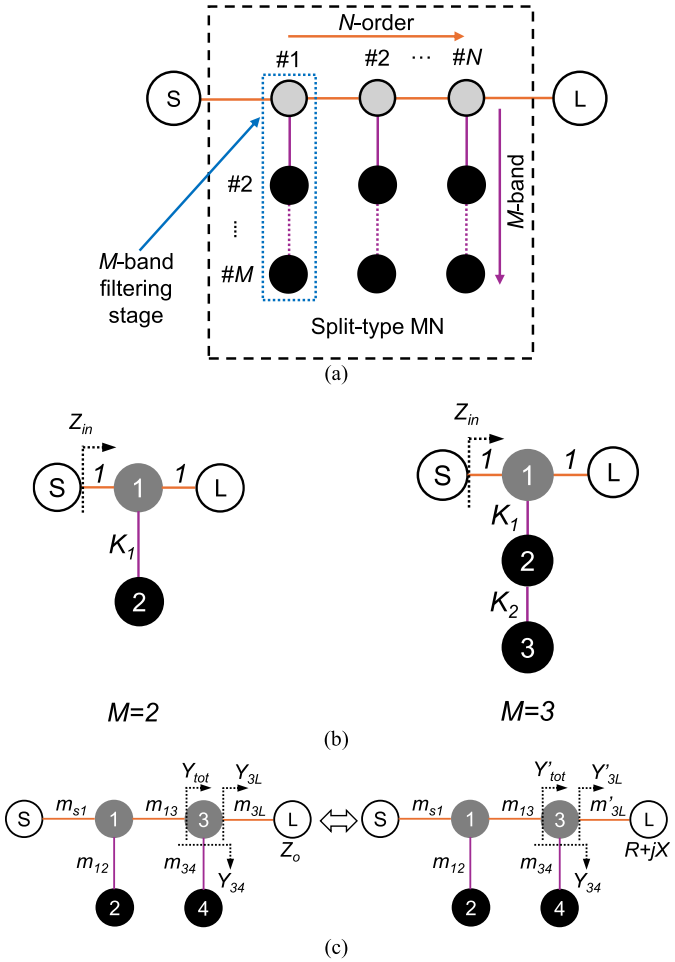

Fig. 2. (a) Coupling routing diagram (CRD) of the M-band N^{th}-order split-type filter matching network. Grey circles: in-line resonators, black circles: in-parallel resonators, white circles: source and load, orange and purple lines: frequency-independent couplings. (b) CRD of the M-band filtering stage for $M = 2$ and 3. (c) Dual-band second-order example for conventional 50 Ω and arbitrary complex termination of the CRD in (a) where $N = 2$ and $M = 2$.

$$[A] = [\mathrm{R}] + \mathrm{s}\,[\mathrm{U}] + \mathrm{j}\,[\mathrm{M}] \tag{4}$$

In these expressions, the matrix $[A]^{-1}_{i,j}$ denotes the ith row and jth column element of the inverse of matrix $[A]$. $[U]$ is the unity matrix with its first and last elements equal to zero and $[R]$ is the normalized source and load impedance matrix with all other entries being equal to zero.

To better illustrate the process, two example cases of a first-order dual-band ($M = 2$, $N = 1$) and a first-order tri-band ($M = 3$, $N = 1$) stage are considered. For simplicity, the external couplings in Fig. 2(b) are set equal to one. The TF of the first-order dual-band stage is provided in (5) wherein the pole locations p_1, p_2, for the dual-band CRD in Fig. 2(b) can be determined by the roots of the denominator of $|\mathrm{S}_{21}|$ and are listed in (6). The TZ frequencies can be calculated from the roots of the numerator of $|\mathrm{S}_{21}|$ as described in (7) for the dual-band stage. Likewise, the first-order tri-band stage will have TF as in (8), pole locations p_1-p_3 listed in (9) and TZ frequencies as in (10). As shown the pole locations are controlled by the in-parallel coupling coefficients K_1, K_2. The same method can be used to specify the location of poles and TZs for higher number of bands or stages in the filter in a similar manner as described in [48].

$$|S_{21}| = \left|\frac{2s}{s^2 + 2s + K_1^2}\right| \tag{5}$$

$$s_{p1,p2} = \pm|K_1| \tag{6}$$

$$s_{TZ1} = 0 \tag{7}$$

$$|S_{21}| = \left|\frac{2s^2 + 2K_2^2}{s^3 + 2s^2 + \left(K_1^2 + K_2^2\right)s + 2K_2^2}\right| \tag{8}$$

$$s_{p1,p3} = \pm\sqrt{K_1^2 + K_2^2} \quad s_{p2} = 0 \tag{9}$$

$$s_{TZ1,TZ2} = \pm|K_2| \tag{10}$$

To demonstrate the operating principles of the split-type MBF-MN, the dual-band second-order example in Fig. 2(c) is considered. Its corresponding synthesized transfer functions are shown in Fig. 3(a) for various band separations. In this case, only the in-parallel coupling elements m_{12} and m_{34} are varied while the CRD is terminated to 50 Ω loads with larger m_{12}, m_{34} values leading to broader stopbands between the two bands. To create a dual-band TF with passbands having dissimilar bandwidths, the self-coupling coefficients m_{22} and m_{44} of resonators 2 and 4 respectively must be altered synchronously such that $m_{22} = m_{44} \neq 0$ as shown in Fig. 3(b). In terms of order and band scalability, they can be augmented by respectively increasing the number of stages (i.e., N) or the number of the resonators (i.e., M) in each multi-resonant stage as shown in Fig. 3(c) and (d) that present synthesized examples for second, third, and fourth order and dual-, tri-, and quad-band TFs respectively. Considering that in practical realization scenarios the resonators exhibit a finite quality factor (Q) that in turn leads to insertion loss (IL) in the passband of a BPF, Fig. 3(e) shows the effect of finite Q factor in the synthesized dual-band response. As expected, the lower the Q, the higher the IL. For Q values ranging from 100 to 200, the IL varies from 2 dB to 1 dB respectively.

A. Complex-Terminated Multi-Band Filter Matching Network

Since the split-type configuration needs to be directly connected to the transistor, it would need to be designed for a complex input and a 50 Ω output impedance so that it maximizes the gain or the NF of the LNA. This is different to conventional BPF design approaches that are designed for 50 Ω. To best elaborate on this, let us consider the example case of the second-order dual-band CRD in Fig.2(c) when terminated to a load with impedance equal to the system's reference impedance (equal to 50 Ω) and in this case the total admittance (Y_{tot}) seen by resonator 3 can be calculated by (11). When an arbitrary load $Z_L = R + jX$ Ω is presented at the output, the new admittance seen by resonator 3 (Y'_{tot}) can be calculated using (12). To maintain the same TF, (11) and (12) need to be equivalent which can be achieved by modifying the coupling coefficient between resonator 3 and the load (m'_{3L}) and adding an additional reactance B as described in (13). As a result, the modified coupling coefficients can be calculated using (14) and (15). To validate this methodology, the synthesized S-parameters of a dual-band BPF using the

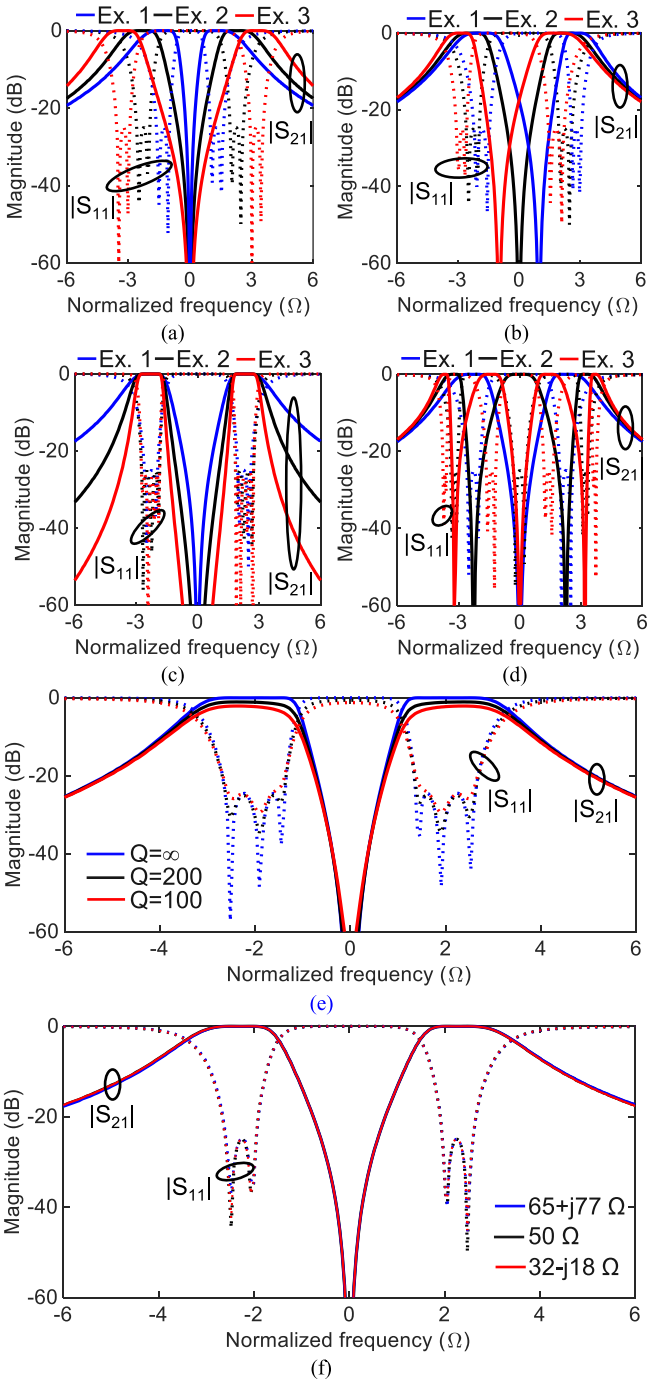

Fig. 3. (a) Synthesized responses for the CRD in Fig. 2(c) for different band separations. Examples 1, 2, and 3: $m_{12} = m_{34} = 1.3$, 2.3, and 3.3 respectively. (b) Synthesized responses for the CRD in Fig. 2(c) for asymmetric passbands. Examples 1, 2, and 3: $m_{22} = m_{44} = -1$, 0, 1 respectively. (c) Synthesized responses for the CRD in Fig. 2(a) for high order TFs. Examples 1, 2, and 3: $M = 2$ and $N = 2$, 3, and 4 respectively. (d) Synthesized responses for increasing the number of bands. Examples 1, 2, and 3: $N = 2$ and $M = 2$, 3, and 4 respectively. (e) Synthesized response of the CRD in Fig. 2(c) for varying resonator Q. (f) Synthesized response for different load terminations. For all examples, $m_{s1} = m_{3L} = 1.15$, $m_{13} = 1.4$, $m_{12} = m_{34} = 2.3$, $m_{11} = m_{22} = m_{33} = m_{44} = 0$, unless stated otherwise.

split-type CRD in Fig. 2(c) are plotted in Fig. 3(f) for a conventional 50 Ω termination and for two alternative complex terminations having an impedance of 65+j77 Ω and 32-j18 Ω. As shown, for any arbitrary load termination, an identical TF is obtained by modifying the corresponding coupling coefficients (i.e. $M'_{3L} = 1.01$ and 1.44 and $M'_{33} = -1.57$ and 0.74 for load terminations of 65+j77 Ω and 32-j18 Ω respectively). Thus, this method can be used for matching the transistor of the LNA while achieving dual-band filtering.

$$Y_{tot} = (m_{3L})^2 \cdot Z_o + Y_{34} \tag{11}$$

$$Y'_{tot} = (m_{3L})^2 \cdot (R + jX) + Y_{34} \tag{12}$$

$$Y'_{tot} = \left(m'_{3L}\right)^2 \cdot (R + jX) + jB + Y_{34} \tag{13}$$

$$m'_{3L} = m_{3L} \cdot \sqrt{Z_o/R} \tag{14}$$

$$B = -X \cdot \left(m'_{3L}\right)^2 \tag{15}$$

Furthermore, this methodology can be readily extended to TFs with an arbitrary number of bands without needing to alter its configuration or coupling coefficients. This is due to the increase of M only affecting Y_{34} which is independent of m'_{3L}. Hence, regardless of the desired number of bands, only a single coupling coefficient needs to be altered in relation to the conventional split-type MBF-MN design. In terms of order scalability, this can be readily obtained by increasing the number of stages N until the required selectivity is reached and by only modifying the external coupling coefficient from the last resonator to the load m'_{NL} and the self-coupling coefficient of the last resonator m'_{nn} using (14),(15).

III. Multi-band Filtering/Diplexer LNAs

The split-type multi-band complex MN concept can be exploited for the realization of multi-band single- and double-ended complex-terminated MNs which can be used to create RF components with multi-functional capabilities, namely MBF-LNAs and MBD-LNAs as shown in Fig. 4(a)-(c). In particular, three different circuit configurations are considered for multi-band operability in common 5G bands. Namely, the: i) MBF-LNA I: dual-band filter LNA with two passbands centered at 2.5 and 3.3 GHz covering the n-7, 30, 38 and n-48,78 5G bands respectively. It is implemented using a conventional IMN and a split-type dual-band MN at the output of the transistor as shown in Fig. 4(a), ii) MBF-LNA II: dual-band filter LNA with passbands centered at 2.5 and 3.3 GHz covering n-7, 30, 38 and n-48,78 bands respectively and enhanced selectivity using a split-type MN at both the input and the output of the transistor as shown in Fig. 4(b), and iii) MBD-LNA: LNA diplexer with two dual-band output channels (Channel 1: passbands centered at 2.4 GHz and 3.3 GHz covering n-30,40,97 and n-77,78 respectively and Channel 2: passbands centered at 2.85 GHz and 3.75 GHz covering n-7, 38,41 and n-77,78) having a conventional IMN and two dual-band split-type complex-terminated MN at its two output as depicted in Fig. 4(c).

A. LNA Core

To start the design process, a low noise BJT transistor is selected and is set in a common emitter configuration as shown in the the LNA core in Fig. 4(d). In this case the low noise transistor BFP840FESD from Infineon is used and is biased using two independent power supplies of $V_b = 1.1$ V and $V_c = 2.1$ V through an RF choke and a base resistance R_b.

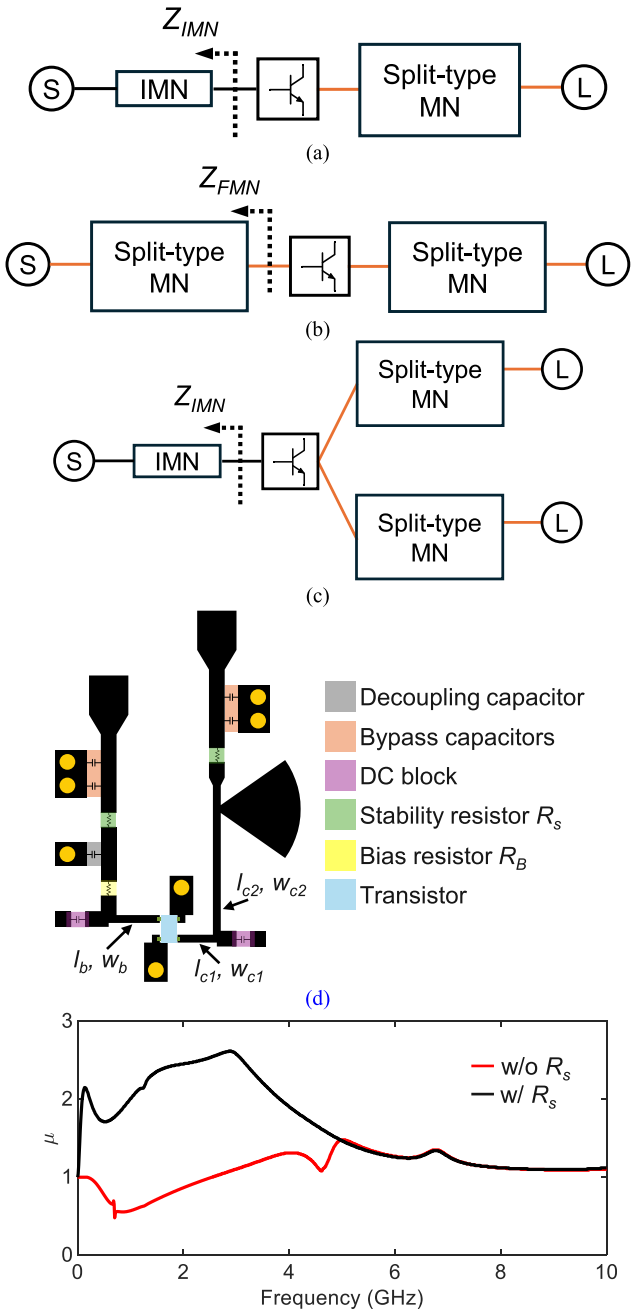

Fig. 4. (a) MBF-LNA I having a conventional MN at the input of the transistor and a split-type MN at the output of the transistor. (b) MBF-LNA II with splittype MNs at both the input and the output of the transistor. (c) MBD-LNA with a conventional MN at the input of the transistor and two split-type MNs at the output. (d) Layout of the LNA core including DC biasing and stability networks. Dimensions and component values are as follows: lb = 1.8 mm, lc1 = 1.4 mm, lc2 = 6 mm, wb = wc1 = wc2 = 0.4 mm, RB = 15 kΩ, Rs = 50 Ω, decoupling capacitor = 39 pF, bypass capacitors = 0.22 uF and 2.2 uF, and DC blocks = 47 pF. (e) Simulated μ stability criteria of the LNA core.

The biasing point was selected for low NF as indicated in the datasheet and corresponds to a base current I_b of 17.7 uA and collector current I_c of 5.85 mA. With the selected bias condition, the device is potentially unstable at the desired frequency bands of operations as shown in its stability factor (μ) in Fig. 4(e). Hence, resistors R_s need to be added in the DC bias paths to make the overall LNA unconditionally stable (Fig. 4(e)) while having minimal influence on the device's

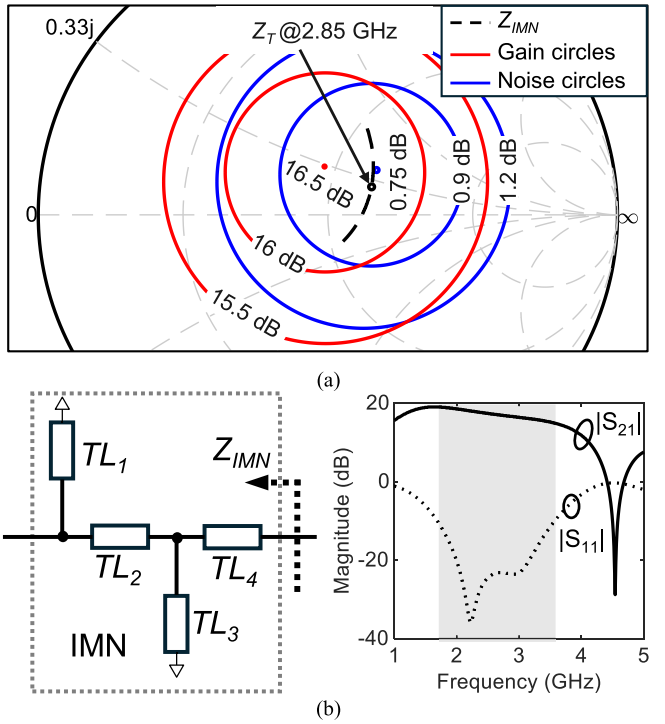

Fig. 5. (a) Constant gain (red) and constant noise (blue) circles of the transistor plotted on a Smith chart alongside the required impedance of the IMN Z_{IMN} and the selected impedance Z_T. Red circles: constant gain circles: 16.5 dB, 16 dB, and 15.5 dB. Blue circles: constant noise circles: 0.75 dB, 0.9 dB, and 1.2 dB. (b) Left: circuit-schematic of the IMN. Dimensions are as follows: TL_1: 105 Ω and 56.1°, TL_2: 35.9 Ω and 4.8°, TL_3: 105 Ω and 106°, and TL_4: 35.9 Ω and 4.8°. Right: S-parameter response of the LNA core using the IMN on the left.

NF. Specifically, an R_s of 50 Ω is selected. In addition, DC blocking capacitors are placed at both the input and output of the LNA core.

Having specified the required circuit elements for biasing and stabilizing the transistor, its input and output impedance loading conditions need to be selected for the desired NF and gain. They are specified through iterative S-parameter circuit-based simulations that generate the constant gain and NF circles at the desired frequency of operation (f_{cen}) as shown in the example case in Fig. 5(a) for f_{cen} = 2.85 GHz. In this figure, the blue circles correspond to the constant NF where the minimum achievable NF is 0.75 dB. Furthermore, the red circles are the constant gain circles with maximum gain of 16.5 dB.

B. MBF-LNA

Considering the two first MN design cases for MBF-LNA I and MBF-II that have bands centered at 2.5 and 3.3 GHz, the f_{cen} for the dual-band MN was chosen to be equal to 2.85 GHz—i.e., the average of the center frequencies of the two bands. As shown in Fig. 5, the optimal matching impedances need to be selected as Z_T = 66.2+j12.7 Ω (black dot in Fig. 5 (a)) for the input load of the transistor and Z_{OMF} needs to be conjugately matched to 58.6-j0.7 Ω for a gain of 15.4 dB, NF of 0.77 dB and input matching of 15 dB. The rest of the parameters are designed as follows:

1) MBF-LNA I: To accommodate the acquisition of all of the 5G sub-bands, a wideband IMN is designed using a

series-shunt stub configuration that matches the Z_T of the transistor equal to a 50 Ω load at the input of the MBF-LNA as depicted in Fig. 5(b). Additionally, due to the shorted quarter-wave line of TL_3 at 4.6 GHz, a TZ is generated at this frequency and can be exploited to increase the TF selectivity of the MBF-LNAs. The resulting Z_{IMN} (dashed black trace) looking into the IMN is shown in Fig. 5(a) and is well aligned with the selected impedance at the design frequency of 2.85 GHz. In this case, the LNA has an input matching of at least 10 dB across the frequency of 1.7 GHz to 3.57 GHz as illustrated in Fig. 5 (b) when its output is terminated with a 50 Ω load. Since the required conjugate match is 58.6-j0.7 Ω, only a slight degradation in gain can be observed when the output is properly matched. In terms of its OMN, the design equations presented in Section II were utilized to match the Z_T of the transistor at 2.85 GHz. Specifically, the split-type OMN is designed for two bands centered at 2.5 and 3.3 GHz and a fractional bandwidth (FBW) of 16 and 12 % respectively. To facilitate these FBWs, a 14% FBW (average between the FBW of the two bands) needs be used in the low-pass-to-bandpass frequency transformation for the calculation of the denormalized coupling coefficients and impedance inverters of the filter which have been calculated using the CRD values in the caption of Fig. 3. Using these as a basis, quarter-wavelength short-circuited resonators, and 90° TL as impedance inverters are implemented.

2) MBF-LNA II: To enhance the selectivity of the MBF-LNA, frequency-selective MNs are used at both the input and output as in MBF-LNA II. In particular, the design of MBF-LNA II is based on MBF-LNA I wherein the conventional IMN is replaced with a split-type IMN. The CRD values of the split-type IMN are calculated based on the CRD described in the caption of Fig. 3 for matching to the impedance Z_T at 2.85 GHz. The resulting S-parameters of the IMN are provided in Fig. 6(a) (Ex. 2) which as it can be seen meet the design requirements. Furthermore, two alternative design examples for the case when f_{cen} is equal to 2.5 GHz and to 3.3 GHz are provided. As shown, for both cases the matching is compromised at the lower and at the higher band respectively. Specifically, the input matching is reduced to 9.5 dB for one of the passbands which shows inefficient power transfer. However, when selecting the average frequency between the bands the same level of matching is obtained for two bands and as such is used for the design of the dual-band split-type MN. Moreover, the achieved matching at both passbands is at least 14 dB which shows sufficient matching and is just 1 dB lower than the targeted matching of 15 dB. The resulting Z_{FMN} (black trace) presented in Fig. 6(b) shows the impedance seen looking into the split-type IMN for the two passbands. In this case, the passband center frequencies are able to achieve a gain of 17.4 dB and 15.7 dB and a NF of 0.87 dB and 0.84 dB for the low and high band respectively. The split-type OMN is designed and implemented in the same manner as MBF-LNA I.

C. MBD-LNA

To facilitate the realization of a single-input dual-output MBD-LNA for multi-antenna systems, two split-type OMN

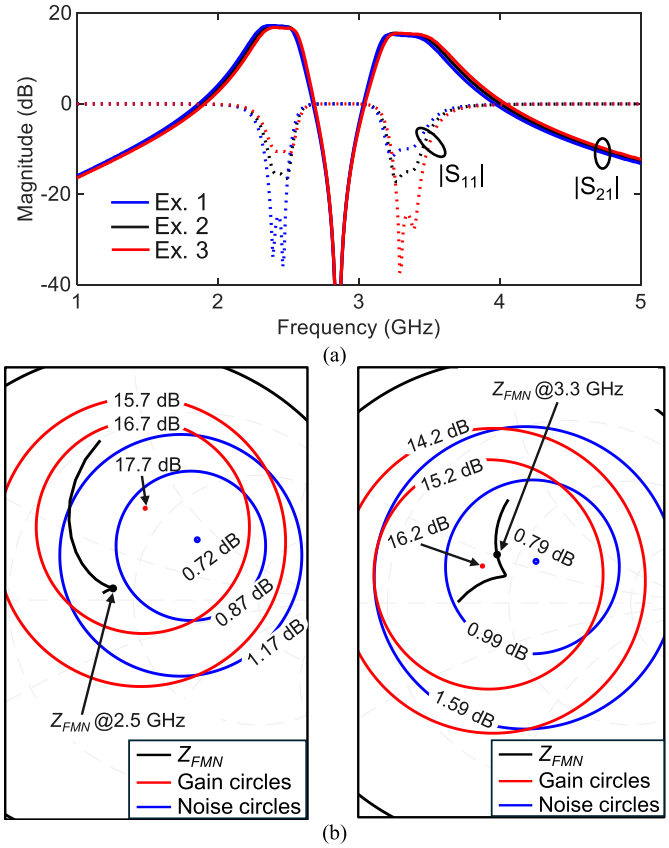

Fig. 6. (a) Simulated S-parameter response of the MBF-LNA in Fig. 4(b) with its IMN designed to match the optimal gain impedance at: 2.4 GHz (Example 1), 2.85 GHz (Example 2), and 3.3 GHz (Example 3). (b) Smith chart showing the constant gain (red) and constant noise (blue) circles of the transistor for the two passband frequencies centered at 2.5 GHz (left) and 3.3 GHz (right).

are connected in a diplexer-like fashion having Channel 1 with passbands centered at bands 1 (2.4 GHz) and 3 (3.3 GHz) and Channel 2 with passbands centered at bands 2 (2.85 GHz) and 4 (3.75 GHz). Due to the wider bandwidth covered by the four bands, the layout and dimensions of the IMN are modified and shown in Fig. 7(a). In particular, length l_3 of the IMN is decreased such that the TZ is moved to 6.6 GHz. The IMN together with the LNA core achieved at least 10 dB matching across the frequency range from 2.0 GHz to 4.55 GHz as depicted in Fig. 7(a).

For increased selectivity in each band, a split-type OMN with $M = 2$ and $N = 3$ is implemented as shown in Fig. 7(b). Utilizing the same methodology as for the complex-terminated split-type filter in Section II, the CRD of the split-type MNs for Channels 1 and 2 are modified such that it conjugately matches the output $Z_{T,out}$ of the LNA core with IMN. The corresponding impedances of $Z_{T,out}$ are 29.2-j2.1 Ω and 27.4-j3.1 Ω at 2.85 GHz and 3.3 GHz respectively. Hence, the modified coupling coefficients for channel 1 are $m_{s,1} = 1.77$ and $m_{1,1} = 0.13$ and Channel 2 are $m_{s,2} = 1.82$ and $m_{2,2} = 0.21$. The diplexer MN is then implemented using a microstrip integration scheme with half-wavelength long TL as impedance inverters and quarter-wavelength short-circuited TLs as resonators. Moreover, the short-circuited stubs/resonators of both the IMN and the split-type OMNs were meandered to reduce the overall size of the circuit.

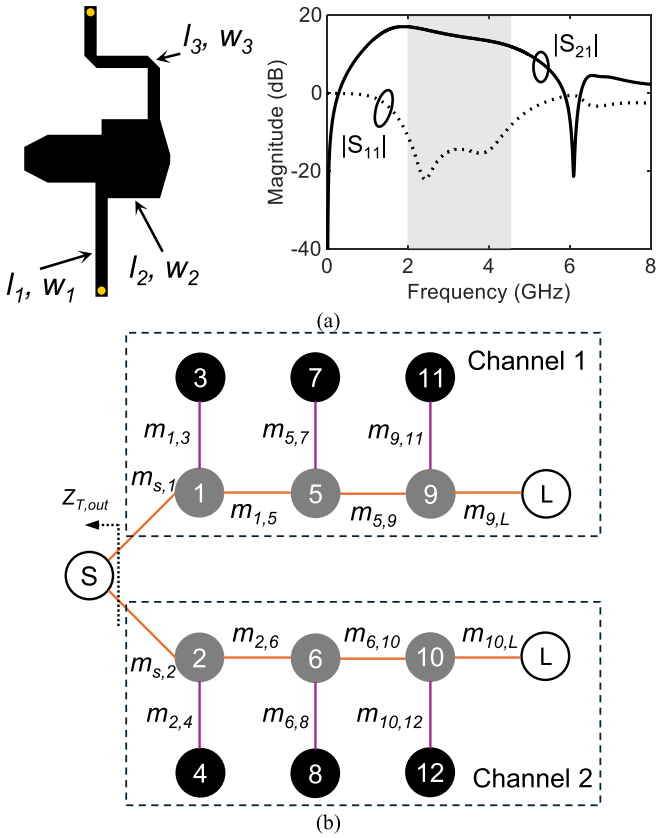

Fig. 7. (a) Left: layout of the IMN for MBD-LNA. Dimensions are as follows: l_1: 9 mm, l_2: 3.9 mm, l_3: 16.6 mm, w_1: 1.2 mm, w_2: 7.7 mm, and w_3: 1.2 mm. Right: S-parameter response of the LNA core using the IMN described on the left. (b) CRD of the split-type diplexer MN. Channel 1: $m_{s,1} = m_{9,L} = 1.35$, $m_{1,5} = m_{5,9} = 1.5$, $m_{1,3} = m_{5,7} = m_{9,11} = 1.9$. Channel 2: $m_{s,2} = m_{10,L} = 1.35$, $m_{2,6} = m_{6,10} = .5$, $m_{2,4} = m_{6,8} = m_{10,12} = 1.9$. All resonators have a self-coupling coefficient equal to zero, $m_{1,1} = m_{3,3} = m_{5,5} = m_{7,7} = m_{9,9} = m_{11,11} = m_{2,2} = m_{4,4} = m_{6,6} = m_{8,8} = m_{10,10} = m_{12,12} = 0$.

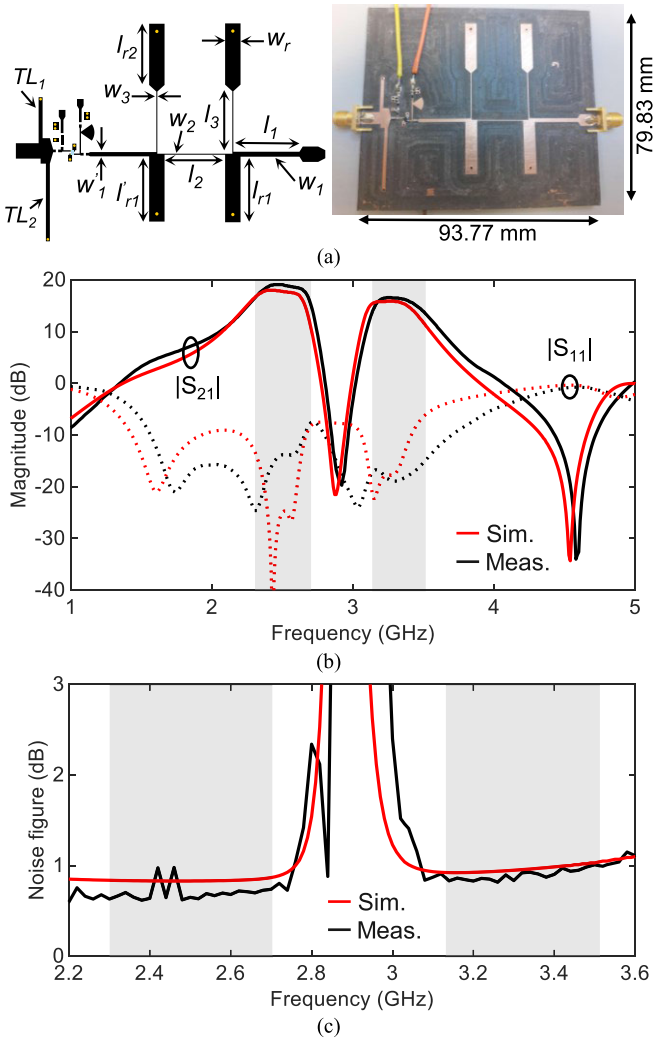

Fig. 8. (a) Layout (left) and manufactured (right) prototype of MBF-LNA I. Dimensions of the filter MN are as follows: TL_1: $l = 12.4$ mm, $w = 1.2$ mm, TL_2: $l = 23.5$ mm, $w = 1.2$ mm, OMN: $l_1 = 17.8$ mm, $l_2 = l_3 = 18.3$ mm, $l_{r1} = 19.83$ mm, $l'_{r1} = 19.73$ mm, $l_{r2} = 18.53$ mm, $w_1 = 1.5$ mm, $w'_1 = 1.3$ mm, $w_2 = w_3 = 0.3$ mm, $w_r = 4.66$ mm. (b) Measured and simulated S-parameter response for MBF-LNA I. (c) Measured and simulated NF of MBF-LNA I.

IV. Experimental Validation

To validate the split-type MBF/MBD-LNA concept, three prototypes, namely the MBF-LNA I, MBF-LNA II and the MBD-LNA were designed, manufactured, and tested. The practical implementation techniques for the resonators and the couplings elements is performed using classic coupled resonator filter design techniques as discussed in [45] and are implemented using quarter-wavelength microstrip transmission lines (TLs). Additionally, a minimum trace width of 0.3 mm is considered in this implementation based on our in-house manufacturing tolerances. All prototypes were built on an RT Duroid 5880 substrate with $\varepsilon_r = 2.2$ and a thickness of 1.57 mm. RF characterization was performed in terms of S-parameters, gain, NF, P_{1dB} and OIP3 using a Keysight PNA-X network analyzer and is discussed in the next sections.

A. MBF-LNA I

The manufactured prototype of the MBF-LNA I is illustrated in Fig. 8(a) and its RF-measured and EM-simulated response are provided in Fig. 8(b)-(c) and Fig. 9. As shown, they are in good agreement successfully validating the proposed concept. The observed discrepancies are attributed to the tolerances of the in-house PCB manufacturing process. Its measured RF performance is summarized as follows: i) low-band: f_{cen}: 2.5 GHz, FBW: 16%, gain: 19.1 dB, minimum input return loss (RL): 10.4 dB, NF: 0.65 dB, OP_{1dB}: -0.59 dBm, and OIP3: 9.9 dBm and ii) high-band: f_{cen}: 3.32 GHz, FBW: 11.7%, gain: 16.5 dB, minimum input RL: 10.16 dB, NF: 0.92 dB, OP_{1dB}: 3.13 dBm, and OIP3: 13.02 dBm. Furthermore, a rejection band with isolation of 37.5 dB is created between the two bands.

B. MBF-LNA II

The layout and experimental prototype of the MBF-LNA II are shown in Fig. 10(a)-(b) and its RF-measured and EM-simulated performance is provided in Fig. 10(c)-(d) and Fig. 11 in terms of S-parameters, NF, 1 dB compression point, and OIP3. As observed, good agreement is achieved between the EM-simulations and the RF-measurements successfully validating the proposed concept. The measured RF

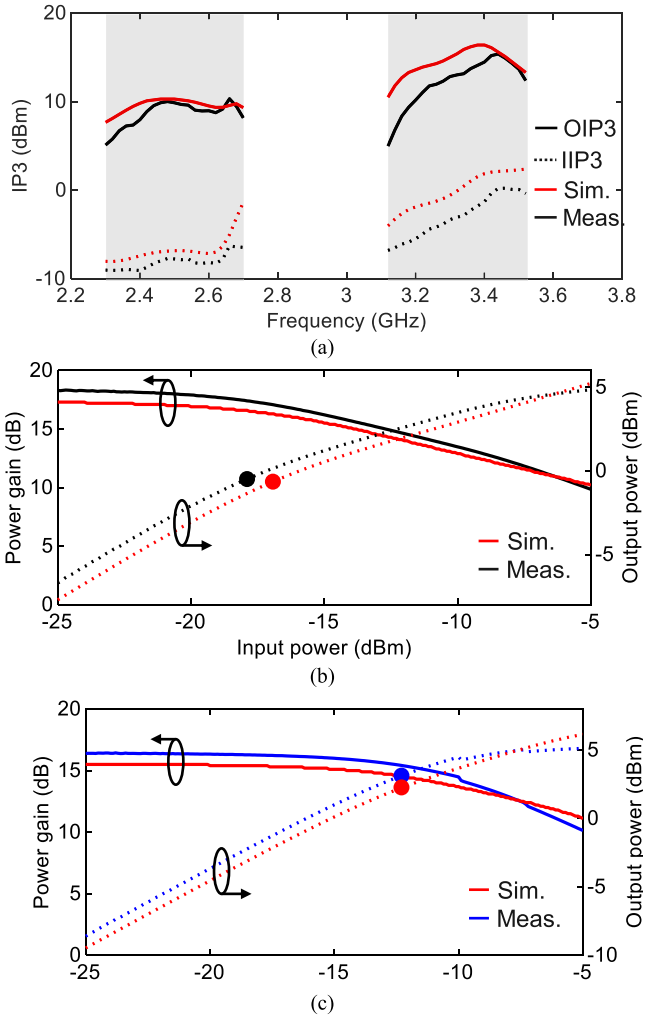

Fig. 9. (a) Measured input (IIP3) and output (OIP3) third-order intercepts of MBF-LNA I. (b) Measured power gain and 1dB compression points of MBF-LNA I at 2.5 GHz. (c) Measured power gain and 1dB compression points of MBF-LNA I at 3.32 GHz.

performance of the MBF-LNA II is summarized as follows: i) low-band: f_{cen}: 2.57 GHz, FBW: 7.8%, gain: 18.3 dB, minimum input RL: 10.07 dB, NF: 1.01 dB, OP_{1dB}: −0.87 dBm, and OIP3: 9.15 dBm and ii) high-band: f_{cen}: 3.26 GHz, FBW: 7.4%, gain: 15.9 dB, minimum input RL: 10.14 dB, NF: 1.52 dB, OP_{1dB}: 1.79 dBm, and OIP3: 14.76 dBm. Due to the use of the split-type MN at both the input and output of the transistor, the rejection band between the two passbands has a significantly higher isolation of 79.5 dB.

C. MBD-LNA

The MBD-LNA has been designed as a single-input dual-channel dual-band diplexer system with this first channel having two passbands centered at 2.4 GHz (band 1) and 3.3 GHz (band 3) and its second channel having two passbands centered at 2.85 GHz (band 2) and 4.75 GHz (band 4). The manufactured prototype of the MBD-LNA is depicted in Fig. 12(a) and its RF-measured and EM-simulated response is provided in Fig. 12(b)-(d) and Fig. 13. Despite the complexity of the circuit, a very good agreement is obtained between the EM-simulated and the RF-measured S-parameters and

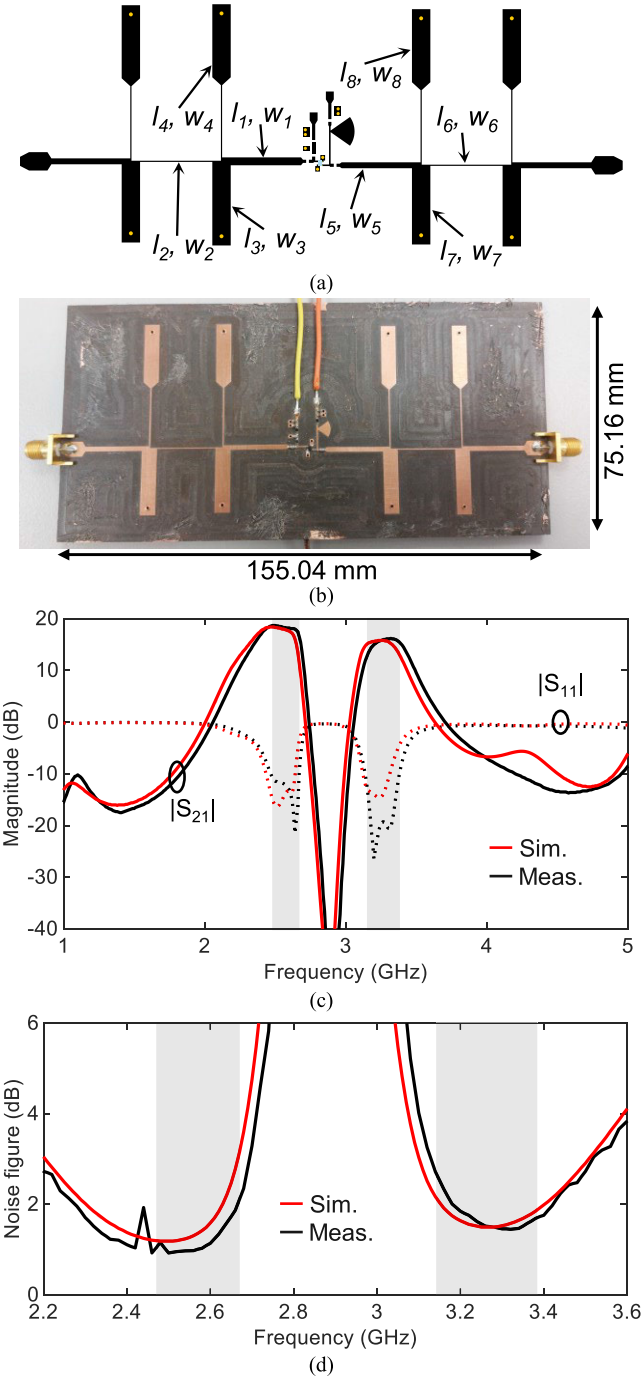

Fig. 10. (a) Layout of MBF-LNA II. Dimensions of the filter MNs are as follows: $l_1 = l_5 = 17.8$ mm, $l_2 = l_6 = 18.3$ mm, $l_3 = l_7 = 19.33$ mm, $l_4 = l_8 = 18.53$ mm, $w_1 = w_5 = 1.5$ mm, $w_2 = w_3 = 0.3$ mm, $w_3 = w_4 = w_6 = w_8 = 4.66$ mm. (b) Manufactured prototype of MBF-LNA II. (c) Measured and simulated S-parameter response of the MBF-LNA II. (d) Measured and simulated NF of the MBF-LNA II.

NF successfully validating the split-type MBD-LNA concept. Specifically, its RF measured performance is summarized as follows: i) Channel 1: band 1: f_{cen}: 2.38 GHz, FBW: 15.55%, gain: 17.17 dB, minimum input RL: 10.85 dB, NF: 0.92 dB, OP_{1dB}: −1.18 dBm, and OIP3: 9.8 dBm, band 3: f_{cen}: 3.29 GHz, FBW: 11.25%, gain: 15.18 dB, minimum input RL: 11.08 dB, NF: 0.93 dB, OP_{1dB}: 1.45 dBm, and OIP3: 12.6 dBm. Furthermore, the maximum rejection between bands 1 and 3 was measured around 43.4 dB.

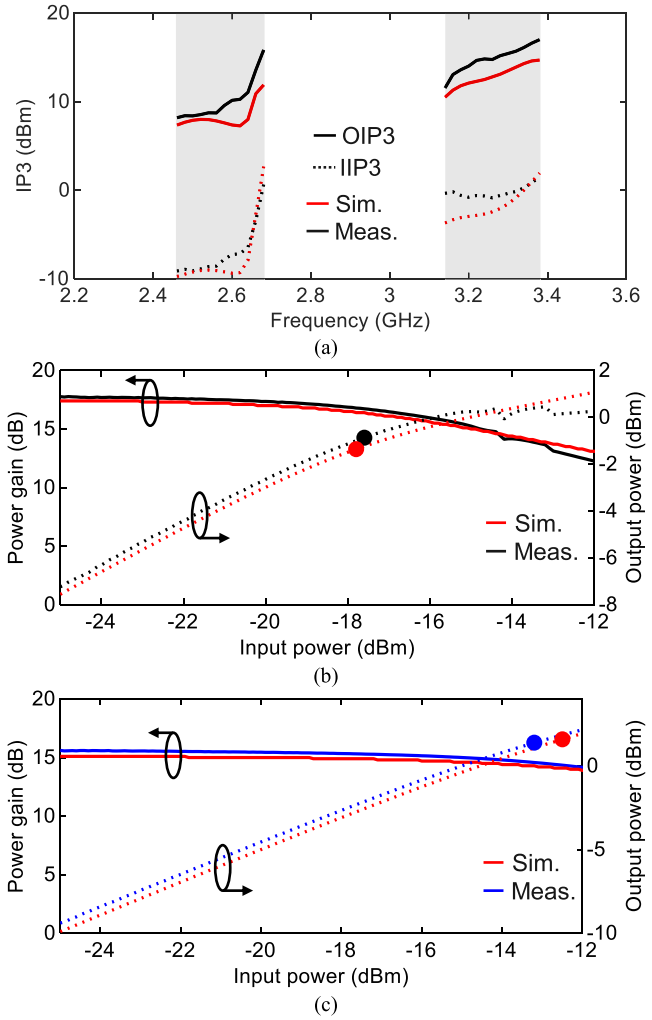

Fig. 11. (a) Measured input (IIP3) and output (OIP3) third-order intercept of MBF-LNA II. (b) Measured power gain and 1dB compression point of MBF-LNA II at 2.57 GHz. (c) Measured power gain and 1dB compression point of MBF-LNA II at 3.26 GHz.

ii) Channel 2: band 2: f_{cen}: 2.82 GHz, FBW: 14.89%, gain: 16.84 dB, minimum input RL: 10.45 dB, NF: 0.87 dB, OP_{1dB}: 0.98 dBm, and OIP3: 6.62 dBm, band 4: f_{cen}: 3.8 GHz, FBW: 11.32%, gain: 14.17 dB, minimum input return loss: 12.17 dB, noise figure: 1.02 dB, OP_{1dB}:1.78 dBm, and OIP3: 11.5 dBm. An isolation of 61.7 dB was measured between bands 2 and band 4. The NF spikes observed in the out-of-band response are due to the presence of 5G signals at these frequencies and insufficient shielding. However, they aren't really of relevance as they are in the out-of-band of the MBD-LNA.

To best situate the merits of the split-type MBF/MBD-LNA concept, Table I compares its performance with the state-of-the-art MB-LNAs and filtering LNAs as the most relevant for this work. Due to the uniqueness of the proposed approach and the lack of MB-LNAs, the comparison spans across alternative integration technologies, from hybrid PCB to GaAs and CMOS. As observed, the proposed concept is the only one that facilitates the realization of compact multi-band LNAs with co-designed multi-band filtering functionality while using a minimum number of components enabled by split-type multi-resonant stages. Furthermore, the potential to realize a dual-band diplexer with LNA capabilities is demonstrated

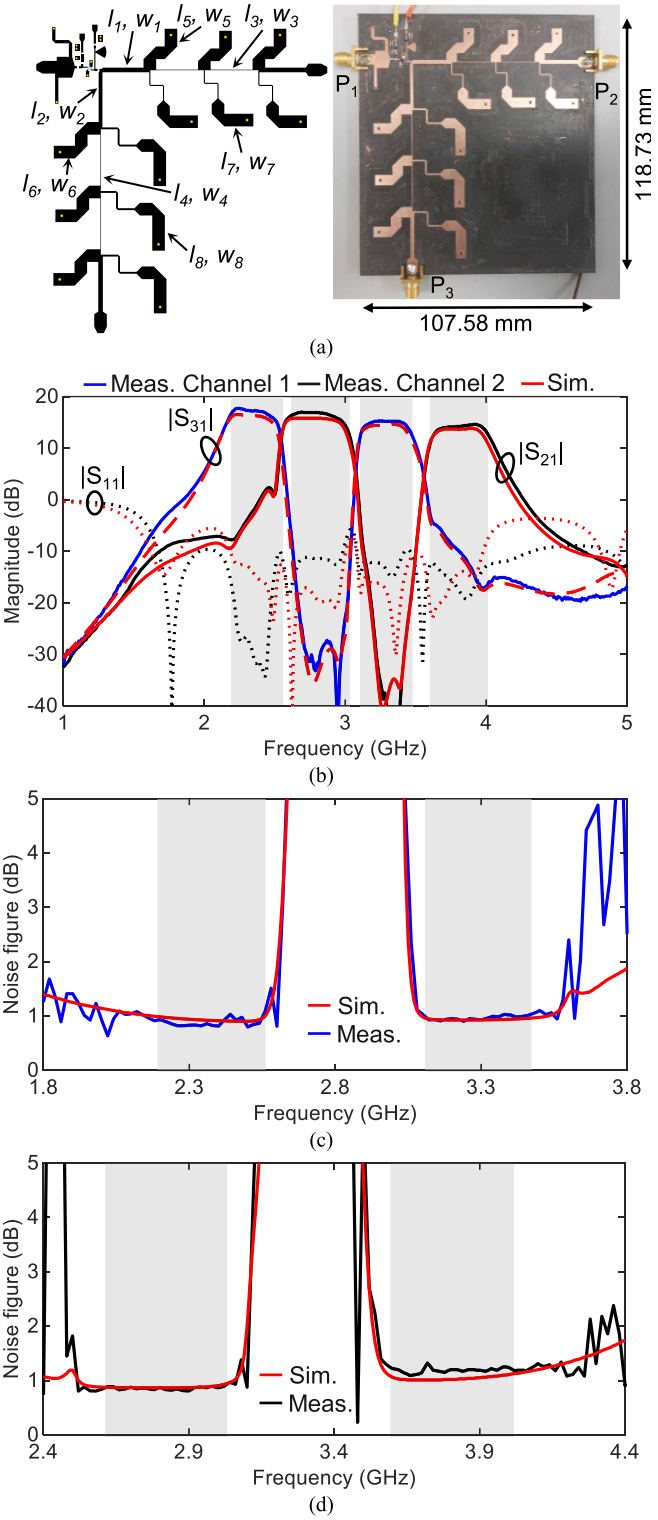

Fig. 12. (a) Layout (left) and manufactured (right) prototype of the proposed MBD-LNA. Dimensions of the split-type diplexer MN are as follows: l_1 = 15 mm, l_2 = 18.3 mm, l_3 = 15.5 mm, l_4 = 18.8 mm, l_5 = 10.5 mm, l_6 = 13.7 mm, l_7 = 12 mm, l_8 = 15.2 mm $w_1 = w_2$ = 1.7 mm, $w_3 = w_4$ = 0.2 mm, $w_5 = w_6 = w_7 = w_8$ = 4.66 mm. (b) Measured and simulated S-parameter response for MBD-LNA. (c) Measured and simulated NF of MBD-LNA at channel 1. (d) Measured and simulated NF of MBD-LNA at channel 2.

in this work for the first time alongside the realization of the highest number of bands (4 as opposed to 1 or 2 in [28], [29], [30], [31], [34], [39], [40], and [41]) and the

TABLE I
COMPARISON WITH STATE-OF-THE-ART MULTI-BAND AND FILTERING LNAS

	Tech.	Fil-ter?	No. of bands	No. of re-son.	Freq. (GHz)	FBW (%)	RL (dB)	Gain (dB)	NF (dB)	OIP3 (dBm)	DC Power (mW)	Band iso. (dB)	Size (λ_g^2)
T.W.	M.S.	Y/O	4	6	2.38/3.29 2.82/3.8	15.6/11.3 14.9/11.3	10.9/11.1 10.5/12.2	17.2/15.2 16.8/14.2	0.92/0.93 0.82/1.02	9.8/12.6 6.6/11.5	14	43.4 61.7	2.94
T.W.	M.S.	Y/IO	2	4	2.57/3.26	7.8/7.4	10.1/10.1	18.3/15.9	1.01/1.52	9.2/14.8	12	79.5	2.4
T.W.	M.S.	Y/O	2	2	2.5/3.32	16/11.7	10.4/10.2	19.1/16.5	0.65/0.92	9.9/13	13.5	37.5	1.54
[28]	CMOS	N	2	N.A.	2.45/5.25	N.A.	25/15	14/15.5	2.3/4.5	14/21.1	10	43*	N.A.
[29]	CMOS	N	2	N.A.	2.4/5.2	N.A.	16.8/19.4	19.3/17.5	3.2/3.3	-0.8/-0.6	2.4	38*	N.A.
[30]	L.C.	N	2	N.A.	1.1/2.4	48/16.7	15.8/24.1	24.4/20.1	2.6/3.0	24.4/25	108	30*	0.23
[31]	GaAs	N	2	N.A.	26/48	N.A.	7/12	12.5/14.5	2.61/3.41	N.A.	14	6*	0.94+
[34]	SISL	N	2	N.A.	2.45/5.25	N.A.	13/20	28.4/28.8	0.7/1.1	21.8/23.7	36	20*	0.28
[39]	SIW	Y/I	1	3	8	10	<10*	15.18	1.71	27	20	N.A.	1.86
[40]	SIW	Y/IO	1	4	10	N.A.	>15*	9	3*	N.A.	N.A.	N.A.	3.06
[41]	M.S.	Y/IO	1	4	4.72	5.1	11.14	13.76	2.26	N.A.	N.A.	N.A.	1.03

*Estimated from plot. I: input, O: output, LC.: lumped components on PCB, M.S.: microstrip, SIW: Substrate integrated waveguide, N.A: Not available, λ_g: guided wavelength at the average frequency of the pass-bands. +: in mm^2 (LNAs in IC process).

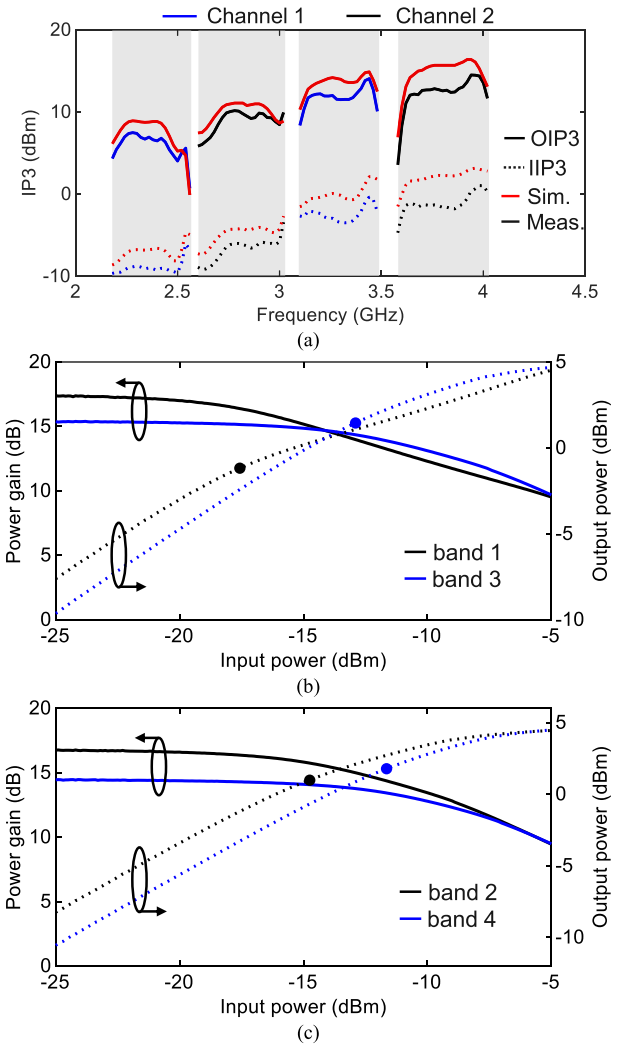

Fig. 13. (a) Measured input (IIP3) and output (OIP3) third-order intercept of MBD-LNA for channels 1 and 2. (b) Measured power gain and 1dB compression point of MBD-LNA at channel 1. (c) Measured power gain and 1dB compression point of MBD-LNA at channel 2.

highest band selectivity. As an additional advantage to be highlighted, the proposed configuration has the lowest power consumption among planar implementations while it realizes bands with comparable gain and the lowest NF while having higher selectivity and significantly higher isolation between its bands. When compared to CMOS approaches, similar NF performance is obtained, however the CMOS concepts in [28] and [29] do not incorporate RF filtering or duplexing as is the case in the proposed approach.

V. CONCLUSION

A comprehensive design methodology and a practical realization scheme is proposed in this work for the first time for the realization of RF co-designed LNAs with multi-band RF filter and diplexer capabilities. Multi-band filtering selectivity is achieved by utilizing split-type multi-resonant stages as complex-terminated matching networks of low noise transistors for the realization of MBF-LNAs and MBD-LNAs. The proposed RF co-designed MBF/MBD-LNA concepts were successfully validated at 5G FR1 frequency bands showing low NF while having high selectivity and high isolation between their bands. Concurrent dual-band operation was demonstrated by two manufactured MBF-LNA prototypes whose performance is summarized as follows: i) MBF-LNA I: NF of 0.65/0.9 dB and gain of 19.1/16.5 dB at 2.5/3.32 GHz, and ii) MBF-LNA II: NF of 1 dB/1.5 dB and gain of 18.3/15.9 dB at 2.57/3.26 GHz. A quad-band MBD-LNA was also manufactured having two output channels with: i) channel 1: NF of 0.92/0.93 dB and gain of 17.2/15.2 dB at 2.38/3.29 GHz, and ii) channel 2: NF of 0.82/1.02 dB and gain of 16.8/14.2 dB at 2.82/3.8 GHz.

ACKNOWLEDGMENT

The authors would like to thank Rogers Corporation for providing the RT 5880 substrate and HITEK for providing the shielding equipment for the NF characterization.

REFERENCES

[1] W. Zhang et al., "Concurrent dual-band receiver based on the multi-port correlator for wireless applications," *IEEE Trans. Circuits Syst. II, Exp. Briefs*, vol. 65, no. 6, pp. 759–763, Jun. 2018.

[2] N. Kumar, K. Rawat, and F. M. Ghannouchi, "Reconfigurable digital delta-sigma modulation transmitter architecture for concurrent multi-band transmission," *IEEE Trans. Circuits Syst. I, Reg. Papers*, vol. 67, no. 7, pp. 2455–2466, Jul. 2020.

[3] S. H. Wang, S. Y. Zheng, K. W. Leung, and M. H. Xia, "A self-matched multi-band rectifier for efficient electromagnetic energy harvesting," *IEEE Trans. Circuits Syst. I, Reg. Papers*, vol. 68, no. 11, pp. 4556–4565, Nov. 2021.

[4] N. Nallam and S. Chatterjee, "Multi-band frequency transformations, matching networks and amplifiers," *IEEE Trans. Circuits Syst. I, Reg. Papers*, vol. 60, no. 6, pp. 1635–1647, Jun. 2013.

[5] H. Darabi, A. Mirzaei, and M. Mikhemar, "Highly integrated and tunable RF front ends for reconfigurable multiband transceivers: A tutorial," *IEEE Trans. Circuits Syst. I, Reg. Papers*, vol. 58, no. 9, pp. 2038–2050, Sep. 2011.

[6] Y. Wu and K. Ma, "Synthesis design of multiband bandpass filters employing multimode bandstop resonators with star-like topology," *IEEE Trans. Circuits Syst. I, Reg. Papers*, vol. 70, no. 6, pp. 2612–2624, Jun. 2023.

[7] M. Malki, L. Yang, and R. Gómez-García, "Input-reflectionless quasi-elliptic-type single- and dual-band bandpass filters based on passive channelized principles," *IEEE Trans. Circuits Syst. I, Reg. Papers*, vol. 70, no. 1, pp. 190–202, Jan. 2023.

[8] D. Simpson and D. Psychogiou, "GaAs MMIC nonreciprocal single-band, multi-band, and tunable bandpass filters," *IEEE Trans. Microw. Theory Techn.*, vol. 71, no. 6, pp. 2439–2449, Jun. 2023.

[9] L. Gao, T. Lin, and G. M. Rebeiz, "Design of tunable multi-pole multi-zero bandpass filters and diplexer with high selectivity and isolation," *IEEE Trans. Circuits Syst. I, Reg. Papers*, vol. 66, no. 10, pp. 3831–3842, Oct. 2019.

[10] R. Gómez-García, R. Loeches-Sánchez, D. Psychogiou, and D. Peroulis, "Multi-stub-loaded differential-mode planar multiband bandpass filters," *IEEE Trans. Circuits Syst. II, Exp. Briefs*, vol. 65, no. 3, pp. 271–275, Mar. 2018.

[11] A. Iqbal, J. J. Tiang, S. K. Wong, S. W. Wong, and N. K. Mallat, "QMSIW-based single and triple band bandpass filters," *IEEE Trans. Circuits Syst. II, Exp. Briefs*, vol. 68, no. 7, pp. 2443–2447, Jul. 2021.

[12] R. Gómez-García, R. Loeches-Sánchez, D. Psychogiou, and D. Peroulis, "Single/multi-band wilkinson-type power dividers with embedded transversal filtering sections and application to channelized filters," *IEEE Trans. Circuits Syst. I, Reg. Papers*, vol. 62, no. 6, pp. 1518–1527, Jun. 2015, doi: 10.1109/TCSI.2015.2418838.

[13] C. Çaliskan, M. Yazici, and Y. Gurbuz, "All-pass network and transformer based SiGe BiCMOS phase shifter for multi-band arrays," *IEEE Trans. Circuits Syst. II, Exp. Briefs*, vol. 68, no. 1, pp. 186–190, Jan. 2021.

[14] N. Qi et al., "A dual-channel Compass/GPS/GLONASS/Galileo reconfigurable GNSS receiver in 65 nm CMOS with on-chip I/Q calibration," *IEEE Trans. Circuits Syst. I, Reg. Papers*, vol. 59, no. 8, pp. 1720–1732, Aug. 2012.

[15] N. Bajpai, P. Maity, M. Shah, A. Das, and Y. S. Chauhan, "An ultra-low noise figure and multi-band re-configurable low noise amplifier," *IEEE Trans. Circuits Syst. I, Reg. Papers*, vol. 70, no. 3, pp. 1006–1016, Mar. 2023, doi: 10.1109/TCSI.2022.3229135.

[16] R. A. Shaheen, T. Rahkonen, and A. Pärssinen, "Millimeter-wave frequency reconfigurable low noise amplifiers for 5G," *IEEE Trans. Circuits Syst. II, Exp. Briefs*, vol. 68, no. 2, pp. 642–646, Feb. 2021, doi: 10.1109/TCSII.2020.3014571.

[17] A. A. Nawaz, J. D. Albrecht, and A. Ç. Ulusoy, "A Ka/V band-switchable LNA with 2.8/3.4 dB noise figure," *IEEE Microw. Wireless Compon. Lett.*, vol. 29, no. 10, pp. 662–664, Oct. 2019.

[18] N. M. Neihart, J. Brown, and X. Yu, "A dual-band 2.45/6 GHz CMOS LNA utilizing a dual-resonant transformer-based matching network," *IEEE Trans. Circuits Syst. I, Reg. Papers*, vol. 59, no. 8, pp. 1743–1751, Aug. 2012.

[19] Y.-H. Wang, K.-T. Lin, T. Wang, H.-W. Chiu, H.-C. Chen, and S.-S. Lu, "A 2.1 to 6 GHz tunable-band LNA with adaptive frequency responses by transistor size scaling," *IEEE Microw. Wireless Compon. Lett.*, vol. 20, no. 6, pp. 346–348, Jun. 2010.

[20] B. Ko et al., "A 39/48 GHz switchless reconfigurable low noise amplifier using common gate and coupled-line-based diplexer," *IEEE Trans. Circuits Syst. II, Exp. Briefs*, vol. 70, no. 11, pp. 4028–4032, Nov. 2023.

[21] Z. Wang et al., "A Ka-band switchable LNA with 2.4-dB NF employing a varactor-based tunable network," *IEEE Microw. Wireless Compon. Lett.*, vol. 31, no. 4, pp. 385–388, Apr. 2021.

[22] Y. Lu, K. S. Yeo, A. Cabuk, J. Ma, M. A. Do, and Z. Lu, "A novel CMOS low-noise amplifier design for 3.1- to 10.6-GHz ultra-wide-band wireless receivers," *IEEE Trans. Circuits Syst. I, Reg. Papers*, vol. 53, no. 8, pp. 1683–1692, Aug. 2006.

[23] K.-H. Chen, J.-H. Lu, B.-J. Chen, and S.-I. Liu, "An ultra-wide-band 0.4-10-GHz LNA in 0.18-μm CMOS," *IEEE Trans. Circuits Syst. II, Exp. Briefs*, vol. 54, no. 3, pp. 217–221, Mar. 2007.

[24] P. Qin and Q. Xue, "Compact wideband LNA with gain and input matching bandwidth extensions by transformer," *IEEE Microw. Wireless Compon. Lett.*, vol. 27, no. 7, pp. 657–659, Jul. 2017, doi: 10.1109/LMWC.2017.2711524.

[25] C. Zhao et al., "A K-/Ka-band broadband low-noise amplifier based on the multiple resonant frequency technique," *IEEE Trans. Circuits Syst. I, Reg. Papers*, vol. 69, no. 8, pp. 3202–3211, Aug. 2022.

[26] Y. Hu and T. Chi, "A systematic approach to designing broadband millimeter-wave cascode common-source with inductive degeneration low noise amplifiers," *IEEE Trans. Circuits Syst. I, Reg. Papers*, vol. 70, no. 4, pp. 1489–1502, Apr. 2023.

[27] T. Kitano, K. Komoku, T. Morishita, and N. Itoh, "A CMOS LNA equipped with concurrent dual-band matching networks," in *Proc. IEEE Asia–Pacific Microw. Conf. (APMC)*, Nov. 2017, pp. 566–569.

[28] H. Hashemi and A. Hajimiri, "Concurrent multiband low-noise amplifiers-theory, design, and applications," *IEEE Trans. Microw. Theory Techn.*, vol. 50, no. 1, pp. 288–301, Jan. 2002.

[29] S. Sattar and T. Z. A. Zulkifli, "A 2.4/5.2-GHz concurrent dual-band CMOS low noise amplifier," *IEEE Access*, vol. 5, pp. 21148–21156, 2017.

[30] A. Aneja, X. J. Li, and P. H. J. Chong, "Design and analysis of a 1.1 and 2.4 GHz concurrent dual-band low noise amplifier for multiband radios," *AEU Int. J. Electron. Commun.*, vol. 134, May 2021, Art. no. 153654.

[31] S. Lee et al., "A concurrent 26/48 GHz low-noise amplifier with an optimal dual-band noise matching method using GaAs 0.15 μm pHEMT," *IEEE Trans. Circuits Syst. II, Exp. Briefs*, vol. 71, no. 3, pp. 1096–1100, Mar. 2024.

[32] J. Lee and C. Nguyen, "A K-/Ka-band concurrent dual-band single-ended input to differential output low-noise amplifier employing a novel transformer feedback dual-band load," *IEEE Trans. Circuits Syst. I, Reg. Papers*, vol. 65, no. 9, pp. 2679–2690, Sep. 2018.

[33] A. Kumar and N. P. Pathak, "Coupled stepped-impedance resonator (CSIR) based concurrent dual band filtering LNA for wireless applications," in *IEEE MTT-S Int. Microw. Symp. Dig.*, Hyderabad, India, Dec. 2015, pp. 262–265.

[34] Z. Ke, S. Mou, K. Ma, and F. Meng, "A 0.7/1.1-dB ultra-low noise dual-band LNA based on SISL platform," *IEEE Trans. Microw. Theory Techn.*, vol. 66, no. 10, pp. 4576–4584, Oct. 2018.

[35] J. Lee and C. Nguyen, "A concurrent tri-band low-noise amplifier with a novel tri-band load resonator employing feedback notches," *IEEE Trans. Microw. Theory Techn.*, vol. 61, no. 12, pp. 4195–4208, Dec. 2013.

[36] A. M. Gamal, H. N. Ahmed, and M. A. El-Kfafy, "A quad-band 0.9/1.8/2.45/3.5 GHz, multi-standard, concurrent LNA using a dual-band impedance transformer," in *Proc. Asia–Pacific Microw. Conf. (APMC)*, vol. 1, Nanjing, China, Dec. 2015, pp. 1–3.

[37] H.-Y. Li, J.-X. Xu, L. Gao, Q. Xue, and X. Y. Zhang, "24–35 GHz filtering LNA and filtering switch using compact mixed magnetic-electric coupling circuit in 28-nm bulk CMOS," *IEEE Trans. Circuits Syst. I, Reg. Papers*, vol. 70, no. 3, pp. 1071–1082, Mar. 2023.

[38] P. Pech, S. Saron, G. Chaudhary, and Y. Jeong, "X-band filter-amplifier for radio frequency front-end receiver systems," in *Proc. Asia–Pacific Microw. Conf. (APMC)*, Nov. 2022, pp. 698–700.

[39] P. Pech, P. Kim, and Y. Jeong, "Co-design of a low noise amplifier with compact substrate integrated waveguide bandpass filtering matching network," *Int. J. RF Microw. Comput.-Aided Eng.*, vol. 32, no. 12, Oct. 2022, Art. no. e23498.

[40] Y. Gao et al., "Substrate integrated waveguide filter–amplifier design using active coupling matrix technique," *IEEE Trans. Microw. Theory Techn.*, vol. 68, no. 5, pp. 1706–1716, May 2020.

[41] S. M. Cheng and D. Psychogiou, "Multi-functional RF filter with co-designed low noise amplifier and RF switching capabilities," in *Proc. IEEE Int. Microw. Filter Workshop (IMFW)*, Cocoa Beach, FL, USA, Feb. 2024, pp. 5–8.

[42] R. Gómez-García, J.-M. Mu noz-Ferreras, and D. Psychogiou, "Split-type input-reflectionless multiband filters," *IEEE Microw. Wireless Compon. Lett.*, vol. 28, no. 11, pp. 981–983, Nov. 2018.

[43] R. J. Cameron, "Advanced coupling matrix synthesis techniques for microwave filters," *IEEE Trans. Microw. Theory Techn.*, vol. 51, no. 1, pp. 1–10, Jan. 2003.

[44] S. Amari, "Direct synthesis of folded symmetric resonator filters with source-load coupling," *IEEE Microw. Wireless Compon. Lett.*, vol. 11, no. 6, pp. 264–266, Jun. 2001.

[45] J.-S. Hong, *Microstrip Filters for RF/Microwave Applications*, 2nd ed., New York, NY, USA: Wiley, 2011.

[46] J. Lee and K. Sarabandi, "A synthesis method for dual-passband microwave filters," *IEEE Trans. Microw. Theory Techn.*, vol. 55, no. 6, pp. 1163–1170, Jun. 2007.

[47] G. Macchiarella and S. Tamiazzo, "Design techniques for dual-passband filters," *IEEE Trans. Microw. Theory Techn.*, vol. 53, no. 11, pp. 3265–3271, Nov. 2005.

[48] R. Gómez-García, L. Yang, J.-M. Mu noz-Ferreras, and D. Psychogiou, "Single/multi-band coupled-multi-line filtering section and its application to RF diplexers, bandpass/bandstop filters, and filtering couplers," *IEEE Trans. Microw. Theory Techn.*, vol. 67, no. 10, pp. 3959–3972, Oct. 2019.

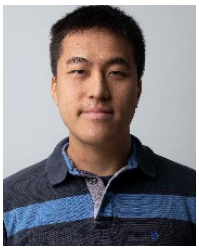

Steven Matthew Cheng (Graduate Student Member, IEEE) received the bachelor's degree in electronics and communications engineering and the master's degree in electrical engineering from the University of the Philippines Diliman, in 2015 and 2017, respectively. He is currently pursuing the Ph.D. degree in electrical and electronic engineering with University College Cork (UCC), Ireland. His current research interests include the design of low noise amplifiers, microwave filters, reconfigurable RF front-ends, and co-integration of RF passive and active components.

Dimitra Psychogiou (Senior Member, IEEE) received the Dipl.-Eng. degree in electrical and computer engineering from the University of Patras, Patras, Greece, in 2008, and the Ph.D. degree in electrical engineering from the Swiss Federal Institute of Technology (ETH), Zürich, Switzerland, in 2013. She is currently a Professor of electrical and electronic engineering with University College Cork (UCC) and the Head of the Advanced RF Technology Group, Tyndall National Institute, Cork, Ireland. Prior to joining UCC, she was a Senior Research Scientist with Purdue University, West Lafayette, IN, USA, and an Assistant Professor with the University of Colorado at Boulder, Boulder, CO, USA. Her current research interests include RF design and characterization of reconfigurable microwave and millimeter-wave passive components, RF-MEMS, acoustic wave resonator-based filters, tunable filter synthesis, frequency-agile antennas, and additive manufacturing technologies for 3D antenna sub-systems. Her research has been presented in more than 250 scientific publications and has received multiple awards, including the 2023 IEEE MTT-S Outstanding Young Engineer Award, the 2021 Roberto Sorrentino Prize, the SFI Research Professorship Award, the 2020 NSF CAREER Award the 2020 URSI Young Scientist Award, and the Junior Faculty Outstanding Research Award from UC Boulder. She is a Senior Member of URSI and a member of the IEEE MTT-S Filters and Passive Components (MTT-5) and Microwave Control Materials and Devices (MTT-13) committees. She is also serving as the President for URSI Ireland, the Vice-Chair for MTT-13, and the Secretary for USNC-URSI Commission D. She is an Associate Editor of the IEEE MICROWAVE AND WIRELESS COMPONENTS LETTERS and the *International Journal of Microwave and Wireless Technologies* and is on the technical review board of various IEEE and EuMA conferences. Previously, she was an Associate Editor of the *IET Microwaves, Antennas and Propagation*.